Ab initio multiconfiguration Hartree-Fock autoionization calculations for ^{21}Sc through ^{27}Ni near the 3*p* excitation edge

K. Nuroh*
Department of Mathematical Sciences, Kent State University, Salem, Ohio 44460, USA
(Received 22 December 2006; published 31 March 2008)

A recently developed theoretical model of random-phase approximation for core-electron scattering in solids has been used to calculate electron-impact excitation relative intensities near the 3*p* excitation edge of the transition metals (TMs), Sc through Ni. To properly reflect the narrow-band character of the valence states of these materials, plus the fact that the $3p \rightarrow 3d$ transitions involved in the analysis are localized, we have employed the nonrelativistic atomic-structure-based multiconfiguration Hartree-Fock (MCHF) approach in the computation of both the ground and continuum states for the otherwise itinerant TM systems.

DOI: 10.1103/PhysRevB.77.125137 PACS number(s): 34.80.Dp, 71.28.+d, 79.20.Fv, 79.20.Uv

I. INTRODUCTION

The unique properties of the 3*d* transition metals (TMs) come from their valence electrons, through the hybridization of the 4*s* and 3*d* states in the free atom. To learn about the electronic structure of these 4*s* and 3*d* states in a solid state environment, experimentalists usually use photons or electrons as probes to induce intra 3*d*-state interactions, as well as interactions of the 3*d* states with core electrons. Spectroscopic measurements of such photon- or electron-initiated interactions in the TMs near the 2*p* and 3*p* excitation edges show structures that are atomic in origin.[1–11] Some atomic-based calculations confirm such a characterization.[12–14] More importantly, as was pointed out in Ref. 1 that while the use of atomic loss-spectroscopic states for the description of the TM atoms in the metal might seem too drastic an assumption compared to, say, treating the *d* states in the tight-binding approximation, such usage is justifiable because both the 3*d*-band width and the 3*p*-3*d* multiplets are small compared with the $3p \rightarrow 3d$ excitation energy. As a consequence, the use of an atomic state wave function for the 3*d* electron instead of a tight-binding one produces the same numbers for quantities such as the Fano asymmetric *q* parameter (as long as matrix elements of the dipole and of the Coulomb matrix elements are neglected between neighboring TM atoms). This is so because such quantities depend on radial integrals involving the $3d \rightarrow \varepsilon f$ transitions that are essentially constant or at most slowly varying in the loss-energy spectrum of interest. From the theoretical standpoint, a TM is an open shell system, and one way to include correlations in the valence band is the use of the multiconfiguration Hartree-Fock (MCHF) as a calculation basis for the electron-impact excitation description of the TMs near their 3*p* excitation edge.

Autoionization emission measurements have been reported for all the 3*d* TMs by electron-impact excitation near the 3*p* excitation edge.[3,15] A major observation of Ref. 3 was that the emission intensity decreased with increasing *Z*. However, the conclusions arrived at in the study of Ref. 15 were spectra of variable spectral widths, intensities, and structures. To investigate these experimental observations, we use a recently developed theoretical model of random-phase approximation for core-electron scattering in solids in Sec. II.[16] In that analysis, the relative intensity yields are formulated in terms of the Fano asymmetric line parameter *q* and energy-loss variable η. In using the formalism in the present investigation, we specifically want to observe any trends in the intensity strengths and resonance widths, as we move across from Sc through Ni. Spin-orbit effects were not included in that formalism. Such magnetic effects will be included in Sec. IV with a reformulation of the problem directly in terms of the Coulomb excitation amplitude and the 3*p*-3*d* multiplets. Finally, the objective of this investigation is twofold. First, we want to apply the results of the theoretical formulation (with and without magnetic effects) to the TMs and point out major calculation differences that exist between the TMs, on the one hand, and La and Ce, on the other. Second, we want to compare the variation of the full width at half maximum (FWHM) of the excitation intensities across the TMs and, also, to comment on how the relative intensity peaks compare with one another and with measurements.[3,15]

II. THEORETICAL BACKGROUND

In order to follow the train of the present calculations, we reproduce the pertinent equations used in the earlier work[16] here, together with any modifications that arise because of the reordering of some variables. Contained in Fig. 1 are the perturbation graphs used in the analysis. The main result of the formulation is the total scattering intensity made up of autoionizing and characteristic decay components given by

$$I(E) \sim (v_{\varepsilon E})^2 R(E),$$

$$R(E) = \left[\frac{\gamma(\eta+q)}{\eta^2+1} + \frac{\gamma' q'(\eta+\Delta\eta)}{(\eta+\Delta\eta)^2+1} \right]^2 + \left[\frac{\eta^2+\eta\gamma q-\gamma+1}{\eta^2+1} + \frac{\gamma' q'(\eta+\Delta\eta)-\gamma'}{(\eta+\Delta\eta)^2+1} \right]^2. \quad (1)$$

In the above and what follows, any parameter or variable without a prime derives from the ring or bubble diagrams. A parameter with a prime is associated with the ladder diagrams, while a parameter with a double prime is connected with the characteristic decay channel.

An analysis based on the Bethe–Born approximation in the theory of inelastic scattering of electrons by atoms

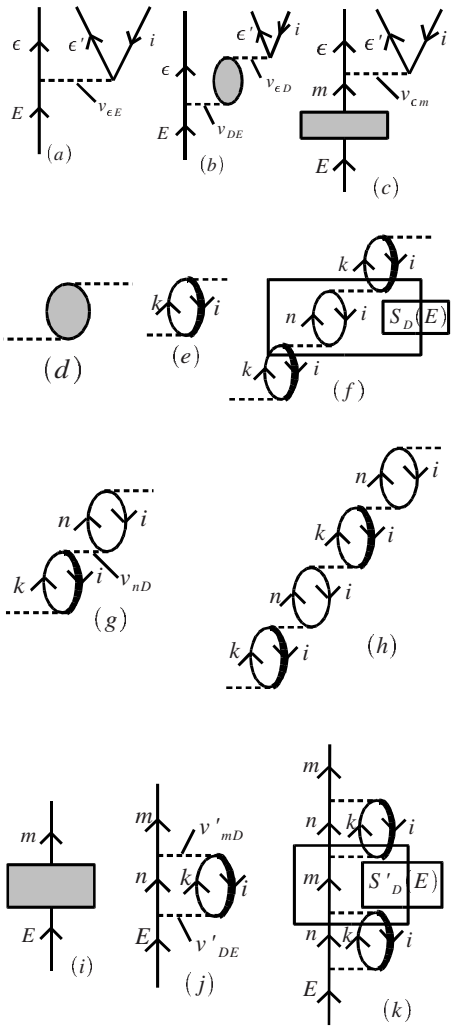

FIG. 1. Amplitude diagrams made up of (a) the basic excitation amplitude, [(b) and (d)–(h)] the resonant contributions from the ring diagrams, [(c) and (i)–(k)] the resonant contributions from ladder diagrams.

showed that the differential scattering cross section is determined essentially by the atomic form factor.[17] This form factor separates into a product of two parts: a nonresonant Born factor and a correlation factor. The nonresonant part is a smoothly varying function of energy that would include the matrix element $(v_{\varepsilon E})^2$ in Eq. (1). Any resonances in the cross section emanate from the correlation part represented here by $R(E)$ in Eq. (1). (Note that the parameter q in the Bethe–Born analysis refers to the momentum transfer and does not have that bearing on its usage in this paper.)

In Eq. (1), q and q' are Fano asymmetric line parameters for the respective autoionizing ring and ladder diagrams defined in terms of Coulomb interactions and are given by

$$q(E) = -\frac{\mathrm{Re}\, V_{\varepsilon D}(E)}{\mathrm{Im}\, V_{\varepsilon D}(E)}, \quad V_{\varepsilon D}(E) = v_{\varepsilon D} + \sum \frac{v_{\varepsilon n} v_{nD}}{E_n - E - i\delta} \tag{2}$$

and

$$q'(E) = -\frac{\mathrm{Re}\, V'_{\varepsilon D}(E)}{\mathrm{Im}\, V'_{\varepsilon D}(E)}, \quad V'_{\varepsilon D}(E) = \sum_n \frac{v'_{\varepsilon n} v'_{nD}}{E_n - E - i\delta}, \tag{3}$$

while η and η' are the corresponding Fano parameters given by

$$\eta(E) = \frac{\mathrm{Re}[E_D - S_D(E) - S''_D(E)]}{\mathrm{Im}[E_D - S_D(E) - S''_D(E)]} \tag{4}$$

and

$$\eta'(E) = \frac{\mathrm{Re}[E'_D - S'_D(E) - S''_D(E)]}{\mathrm{Im}[E'_D - S'_D(E) - S''_D(E)]}, \tag{5}$$

with

$$E_n = E_{nf} + E_{\varepsilon d} - E_{3d}, \quad E'_n = E_{nf} \tag{6}$$

and

$$E_D = E_{\varepsilon d} + E_{3d} - E_{3p}, \quad E'_D = E_{3d} + E_{3d} - E_{3p}. \tag{7}$$

In Eqs. (4) and (5), $S_D(E)$ and $S'_D(E)$ are the interacting self-energies for the autoionizing decay channel for the ring and ladder diagrams, respectively, while $S''_D(E)$ is the self-energy for the characteristic decay channel. These are defined in terms of the bare Coulomb interaction matrix elements as

$$S_D(E) = \sum_n \frac{(v_{Dn})^2}{E_n - E - i\delta}, \quad E_n = E_{nf} + E_{\varepsilon d} - E_{3d}, \tag{8}$$

$$S'_D(E) = \sum_n \frac{(v'_{Dn})^2}{E'_n - E - i\delta}, \quad E'_n = E_{nf}, \tag{9}$$

and

$$S''_D(E) = \sum_n \frac{(v''_n)^2}{E''_n - E - i\delta}, \quad E''_n = E_{nf} - E_{3d} - E_{3d}. \tag{10}$$

Finally, the parameters γ and γ' that appear in Eq. (1) are defined in terms of the bare Coulomb interactions as

$$\gamma = \frac{2\pi (v_{DE})^2}{2\pi[(v_{DE})^2 + (v''_{DE})^2]}, \quad \gamma' = \frac{2\pi (v'_{DE})^2}{2\pi[(v'_{DE})^2 + (v''_E)^2]}, \tag{11}$$

with

$$(v_{DE})^2 = \sum_n (v_{Dn})^2 \delta(E - E_n), \quad (v'_{DE})^2 = \sum_n (v'_{Dn})^2 \delta(E - E'_n),$$

$$(v''_E)^2 = \sum_n (v''_n)^2 \delta(E - E''_n). \tag{12}$$

The explicit Coulomb interactions that appear in Eqs. (1)–(3), and in Eqs. (8)–(12), are given in terms of Slater integrals as

$$v_{\varepsilon E} = \sqrt{6} R^1(3d3d;Ef3p) + (2\sqrt{21}/7) R^3(3d3d;Ef3p), \tag{13}$$

$$(v_{Dn})^2 = 4R^1(3d3d;nf3p)^2 + (24/49) R^3(3d3d;nf3p)^2, \tag{14}$$

$$(v'_{Dn})^2 = (14/15)R^1(3d3d;nf3p)^2 - (24/175)R^1(3d3d;nf3p)R^3(3d3d;nf3p) + (96/1225)R^3(3d3d;nf3p)^2, \quad (15)$$

and

$$(v''_n)^2 = (34/15)R^1(3d3d;nf3p)^2 - (8/35)R^1(3d3d;nf3p)R^3(3d3d;nf3p) + (16/35)R^3(3d3d;nf3p)^2. \quad (16)$$

Note that $E_{\varepsilon d} \equiv E_{3d}$, and this makes $E_n = E'_n$. We also note that in Eq. (1), $(\eta + \Delta\eta)$ replaces $(\eta - \Delta\eta)$ in the original analysis.[16] This is because $\Delta\eta = \eta - \eta'$ was so defined to make $\Delta\eta > 0$ for La and Ce. For the TMs, we have to interchange the roles of η and η' and instead set

$$\Delta\eta = \eta' - \eta = \frac{\mathrm{Re}[E'_D - S'_D(E) - S''_D(E) - E]}{\pi[(v'_{DE})^2 + (v''_E)^2]} - \frac{\mathrm{Re}[E_D - S_D(E) - S''_D(E) - E]}{\pi[(v_{DE})^2 + (v''_E)^2]}. \quad (17)$$

From the numerical computations we would describe later, Re $S_D(E)$ and Re $S'_D(E)$ are negative, while Re $S''_D(E)$ is positive for all the TMs. From the numerical computations we would describe later, Re $S_D(E)$ and Re $S'_D(E)$ are negative, while Re $S''_D(E)$ is positive for all the TMs. Further, $|\mathrm{Re}\, S'_D(E)| \ll |\mathrm{Re}\, S_D(E)|$, $|\mathrm{Re}\, S''_D(E)|$ and $|\mathrm{Re}\, S''_D(E)| - |\mathrm{Re}\, S_D(E)| \cong 0$ but negative. These considerations make the numerators of Eq. (17) positive since $E'_D - E$ and $E_D - E$ are positive when E is set equal to the $3p$ excitation edge energy $E_{3d} - E_{3p}$. However, $[(v'_{DE})^2 + (v''_{DE})^2] \ll [(v_{DE})^2 + (v''_{DE})^2]$, as evidenced from Eqs. (14)–(16). Consequently, when their reciprocals are taken in conjunction with the above analysis, it makes $\Delta\eta$ positive.

We consider some limiting cases of Eq. (1). Since $(v'_{DE})^2 \ll (v_{DE})^2$, we may set $\gamma = 0$. Equation (1) then becomes

$$R_A(E) = \left[\frac{(\eta + \gamma q)^2 + (\gamma - 1)^2}{\eta^2 + 1}\right]. \quad (18)$$

If, further, we set $\gamma = 1$ in Eq. (18), the intensity becomes

$$R_F(E) = (\eta + q)^2/(\eta^2 + 1). \quad (19)$$

Equation (18) describes the physical situation in which characteristic decay events are neglected, and the scattering cross section results from only autoionization events. Equation (19), on the other hand, describes the physical situation whereby the discrete state $3p \rightarrow 3d$ is seen as interacting with the continuum $3d \rightarrow kf$ channel, producing a Fano-like line profile for the intensity. The numerical computations we will consider in the next section would be based on Eqs. (1), (18), and (19), to see what effect the neglect of the ladder diagram contribution would have on the line shapes and strengths of the scattering intensity for the TMs.

TABLE I. Active set of orbitals used in MCHF and CMCHF routines for each atom. The pairs of numbers in the last two columns indicate the respective number of configurations and terms generated by the NOHN routine.

Atom	MCHF	CMCHF	MCHF	CMCHF
Sc	$3p,3d$	$3p,3d$	38, 1336	44, 1599
Ti	$3p,3d$	$3p,3d$	28, 931	47, 2193
V	$3p,3d$	$3p,3d$	11, 221	41, 2843
Cr	$3p,3d,4p$	$3p,3d,4p$	51, 3730	54, 3838
Mn	$3p,3d,4p$	$3p,3d,4p$	92, 8562	95, 8667
Fe	$3p,3d,4s$	$3p,3d$	4, 77	25, 1985
Co	$3p,3d,4s$	$3p,3d$	3, 19	31, 2642
Ni	$3p,3d,4s$	$3p,3d$	1, 16	20, 1303

III. COMPUTATIONAL DESCRIPTION

A. MCHF and CMCHF calculations

In the electron-impact excitation process, an incident electron of energy E scatters off a transition metal, which is represented here by the atom in its ground state. The ground state is partitioned into a core-electron configuration $1s^2 2s^2 2p^6 3s^2$ and a pseudovalence electron configuration $3p^6 3d^1 4s^2(^2D)$ for Sc, $3p^6 3d^2 4s^2(^3F)$ for Ti, $3p^6 3d^3 4s^2(^4F)$ for V, $3p^6 3d^5 4s^1(^7S)$ for Cr, $3p^6 3d^5 4s^2(^6S)$ for Mn, $3p^6 3d^6 4s^2(^5D)$ for Fe, $3p^6 3d^7 4s^2(^4F)$ for Co, and $3p^6 3d^8 4s^2(^3F)$ for Ni. The key ingredient to performing the numerical calculations outlined in the previous section is the knowledge about the continuum Slater integrals $R^{1,3}(3d3d;kf3p)$ where $E = k^2/2$ (in a.u.), where 1 a.u. $= 27.2$ eV. We use the MCHF codes to determine these continuum integrals. The MCHF approach to computational atomic structure has been shown to provide better atomic one-electron properties than the HF method.[18–21] The philosophy behind its development is to induce as much correlation effects in the outer subshells of an atomic system as possible. This makes it even more reflective of open shell systems such as the $3d$ TM atoms, where inter- and intraconfiguration interactions are important to properly describe the narrow valence bands. It is for this reason, in part, why we employ the MCHF approach in determining the radial wave functions.

The initial objective was to include the set of orbitals $\{3p,3d,4s,4p\}$ as the active set for the generation of the configuration list by the GENCL routine. This list would serve as an input for the NONH routine to set up the energy interactions for the MCHF routine to self-consistently calculate the energies and radial wave functions, using the HF energies and radial wave functions as initial estimates. Inclusion of all the four orbitals would sometimes make the self-consistent iterations in the MCHF code nonconvergent. In a series of trial and error attempts, the active set of orbitals shown in Table I were the minimal set capable of producing convergence in the iterative procedures in the MCHF and CMCHF routines. The common core-electron configuration of $1s^2 2s^2 2p^6 3s^2$ was used for all the TM atoms for the perturber and the perturber plus the continuum electron. The pairs of numbers

TABLE II. The $3p$- and $3d$-subshell ionization energies (a.u.); 1 a.u.=27.2 eV.

		E^i_{3p}		E^i_{3d}		CMCHF	
Atom	Configuration	HF	MCHF	HF	MCHF	E^i_{3p}	E^i_{3d}
Sc	$3p^6 3d 4s^2(^2D)$	3.149097	3.147770	0.687424	0.674958	3.148759	0.683290
Ti	$3p^6 3d^2 4s^2(^3F)$	3.590175	3.587478	0.881312	0.872311	3.589803	0.879998
V	$3p^6 3d^3 4s^2(^4F)$	4.038455	4.034562	1.019241	1.010780	4.038190	1.018654
Cr	$3p^6 3d^5 4s(^7S)$	4.101869	4.105219	0.747210	0.750428	4.096089	0.741386
Mn	$3p^6 3d^5 4s^2(^6S)$	4.959052	4.952845	1.277694	1.268607	4.952052	1.270529
Fe	$3p^6 3d^6 4s^2(^5D)$	5.484382	5.478590	1.293766	1.285394	5.490568	1.300658
Co	$3p^6 3d^7 4s^2(^4F)$	6.012496	6.014784	1.350840	1.352847	6.014784	1.352847
Ni	$3p^6 3d^8 4s^2(^3F)$	6.555352	6.555360	1.413851	1.413865	6.555360	1.413863

in the last two columns of Table I indicate the respective number of configurations and terms, and hence the dimensionality used in the eigenvalue problem for the energy matrices. In Table II, we report the $3p$- and $3d$-binding energies from the HF and MCHF calculations for comparison. (These energies are also denoted by E^i_{3p} and E^i_{3d} in Table II.) However, the MCHF values were the ones used for any computation that involves the $3p$- and $3d$-binding energies.

B. Intensity calculations

Once the continuum Slater integrals $R^{1,3}(3d3d;kf3p)$ are determined, the parameters γ and γ' are evaluated directly from Eqs. (11)–(16). These parameters are energy dependent, so they have been evaluated at the $3p$-$3d$ excitation energy $E=E_{3d}-E_{3p}$. In fact, all energy-dependent quantities are evaluated at this excitation energy. The determination of the parameters q, q', and $\Delta\eta$ involves principal value sums or, equivalently, integrals of the form $P\int f(E')dE'/(E'-E)$. The functions $f(E)$ are all positive definite. The variation of $(v_{\varepsilon E})^2$ with energy E from Eq. (13) is displayed in Figs. 2 and 3 for Sc through Ni.

The reason for presenting Figs. 2 and 3 is twofold. First, each of the curves would be part of the nonresonant atomic Born factor. They would essentially provide the excitation cross sections if autoionization and characteristic decay mechanisms were excluded. Second, the integrand function $f(E)$, used in the principal value integrations, assumes one of the following forms: $v_{\varepsilon E}v_{ED}$, $(v_{DE})^2$, $v'_{\varepsilon E}v'_{ED}$, $(v'_{DE})^2$, or $(v''_E)^2$. Each one of these quadratic interaction functions has a distribution profile similar to Figs. 2 and 3 for the various atoms but with different strengths. All such distributions fit excellently to a log-normal function defined by the equation

$$y(x) = y_0 + \frac{A}{\sqrt{2\pi}wx} e^{-[\ln(x/x_c)]/2w^2}, \tag{20}$$

where y_0 is the offset parameter, x_c is the center of the distribution, and A and w are the respective amplitude and width of the distribution. With the various interactions $v_{\varepsilon E}v_{ED}$, $(v_{DE})^2$, $v'_{\varepsilon E}v'_{ED}$, $(v'_{DE})^2$, and $(v''_E)^2$ serving as integrands represented by a fitted form of Eq. (20), the principal value integrations were numerically obtained using the quadrature QAWC from the GNU SCIENTIFIC LIBRARY.[22] Every such computed principal value integral was negative except those involving $(v''_E)^2$ that were positive. This is because the singularity in the principal value integration for all the other integrands is at $E=E_{3d}-E_{3p}$, while for $(v''_E)^2$, the singularity occurs at $E=3E_{3d}-E_{3p}$. The results of the final calculations for q, q', and $\Delta\eta$, together with γ and γ' are presented in Table III. With the values of the parameters from Table III, the relative intensities for the TMs are calculated as a function of the energy-loss parameter η using Eq. (1). The results of the calculation are presented in Fig. 4.

When Eq. (18) is used to calculate the autoionizing intensities, they produced results that were virtually identical with the ones presented in Fig. 4, both in shape and in strength. Using Eq. (19), the Fano formula produced intensities that were about 1.8 times smaller in strength for all the TMs. Rather than presenting the intensity profiles from the latter two calculations, we show instead their maximum strengths in Table IV in comparison with the maximum strengths from Fig. 4. In Table IV, we also present the FWHM values of the

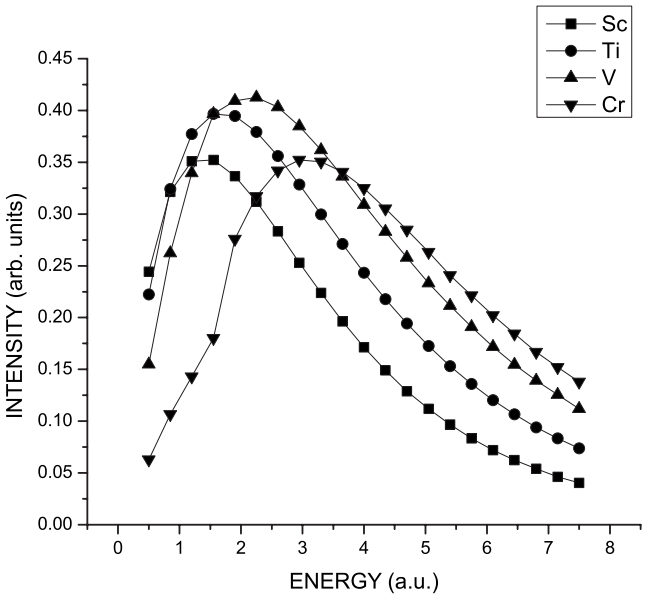

FIG. 2. The variation of the nonresonant matrix element $(v_{\varepsilon E})^2$ with energy for Sc through Cr (1 a.u.=27.2 eV).

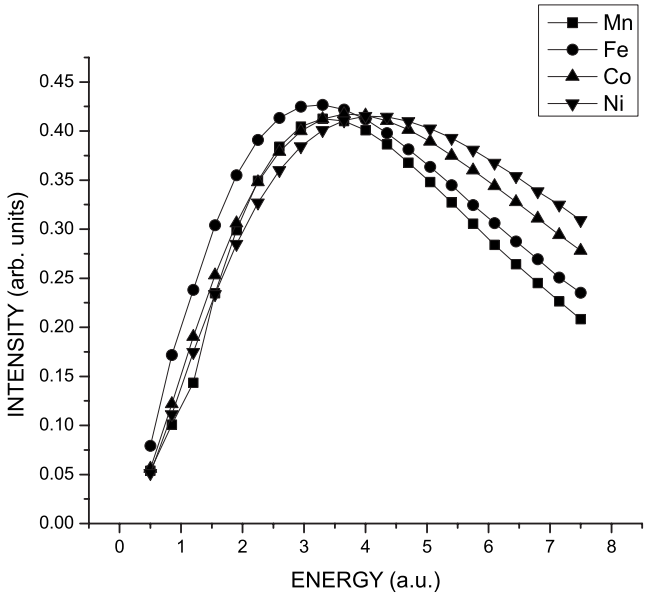

FIG. 3. The variation of the nonresonant matrix element $(v_{\varepsilon E})^2$ with energy for Mn through Ni (1 a.u.=1 27.2 eV).

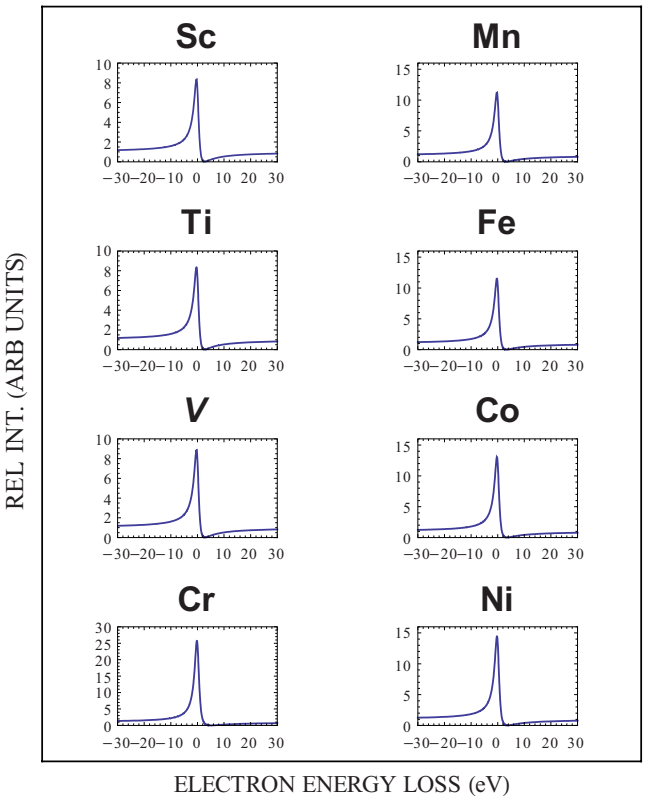

FIG. 4. (Color online) The relative intensities (arb. units) for the TMs using $R(E)$ from Eq. (1).

spectra. These were determined using a Gaussian fit to the data. We observe that the FWHM values are about the same for all the TMs whether Eq. (1), (18), or (19) is used to represent the energy-loss spectra. From the intensity perspective, the data suggest that the autoionizing events virtually dominate the spectra. Consequently, the model suggests that the simpler autoionizing formula contained in Eq. (18) is sufficient and should be used in describing energy loss spectra of the TMs.

IV. FORMULATION WITH MAGNETIC EFFECTS

A. Energy matrices

The discussion in the previous sections has been done without spin-orbit interaction effects and the only energy parameters considered were the electrostatic energies of the $3p$ and $3d$ states E_{3p} and E_{3d}. Inclusion of such magnetic effects would require the spin-orbit energy parameters ς_{3p} and ς_{3d} and the Slater integrals $F^k(3p,3d)$ and $G^k(3p,3d)$ in the calculation of the excited state energies of the transitions $3p^6 3d^n 4s^2 \rightarrow 3p^5 3d^{n+1} 4s^2$ for Sc through Ni and the transition $3p^6 3d^5 4s \rightarrow 3p^5 3d^6 4s$ for Cr. Since $\varsigma_{3d} \ll \varsigma_{3p}$, spin-orbit contributions from the $3d$ states would be neglected. Further, because $\varsigma_{3p} \ll F^k(3p,3d), G^k(3p,3d)$, the LS or Russell—Saunders coupling scheme would be used in the energy designation of the excited state configurations. Also in the calculation of these energies, the $3p^5$ configuration may be replaced by the $3p$ hole $3\underline{p}$. As a consequence, we will calculate the energies of the excited states of the transitions $3p^6 3d^n 4s^2(S_0 L_0 J_0) \rightarrow 3\underline{p} 3d^{n+1} 4s^2(S' L' J')$ for Sc through Co except Cr and Ni. For Cr, the transition is $3p^6 3d^5 4s(S_0 L_0 J_0) \rightarrow 3\underline{p} 3d^6 4s(S' L' J')$, and for Ni, the transition is $3p^6 3d^8 4s^2(S_0 L J_0) \rightarrow 3\underline{p} 3\underline{d} 4s^2(S' L' J')$. The diagonalization of the direct Coulomb interaction is given by (with $N=n+1$)

TABLE III. Summary of parameters used in calculating the relative intensities, as described in the text.

	Sc	Ti	V	Cr	Mn	Fe	Co	Ni
γ'	0.180769	0.180292	0.180102	0.180487	0.180487	0.180407	0.178477	0.180277
γ	1.411580	1.408971	1.412405	1.411544	1.412361	1.411541	1.411322	1.411545
q'	0.562109	0.463971	0.414667	0.341837	0.225557	0.385617	0.368017	0.379834
q	−1.898164	−1.903562	−1.963037	−3.512248	−2.243301	−2.279779	−2.441642	−2.582100
$\Delta\eta$ (eV)	46.115779	47.588539	48.606247	43.119940	68.165908	58.582108	69.44551	66.454964

$$\Delta E_D(S'L'J') = N\sum_{\substack{\nu SL \\ \bar{\nu}\bar{S}\bar{L}}} \langle \underline{3p}(\ 3d^{N-1}\bar{\nu}\bar{S}\bar{L}|\}3d^N\nu SL) \times [S'L'J']|\sum_{i<j}(r_{ij})^{-1}|\underline{3p}(\ 3d^{N-1}\bar{\nu}\bar{S}\bar{L}|\}3d^N\nu SL)[S'L'J']\rangle. \tag{21}$$

If we denote the coefficient of fractional parentage $(3d^{N-1}\bar{\nu}\bar{S}\bar{L}|\}3d^N\nu SL)$ by $G^{\nu SL}_{\bar{\nu}\bar{S}\bar{L}}$, then the above expression for the energy matrices degenerate in $S'J'$ is evaluated to give the expression

$$\Delta E_D(L') = N\sum_k F^k(3p,3d)\begin{pmatrix} p & k & p \\ 0 & 0 & 0 \end{pmatrix}\begin{pmatrix} k & d & p \\ 0 & 0 & 0 \end{pmatrix} \times [p,d]\sum_{\substack{\nu SL \\ \bar{\nu}\bar{S}\bar{L}}} |G^{\nu SL}_{\bar{\nu}\bar{S}\bar{L}}|^2(-1)^{\bar{L}+L'}[L]\begin{Bmatrix} L & L & k \\ d & d & \bar{L} \end{Bmatrix} \times \begin{Bmatrix} L & L & k \\ p & p & L' \end{Bmatrix}. \tag{22}$$

In the above and the following, $[a,b,\ldots]=(2a+1)(2b+1)\cdots$, and the objects in the brackets and curly brackets represent the $3j$ and $6j$ symbols, respectively. Similarly, by replacing the Coulomb direct interaction in the equation above with its exchange counterpart, the exchange Coulomb energy levels are given by

$$\Delta E_X(L') = N\sum_k G^k(3p,3d)\begin{pmatrix} p & k & d \\ 0 & 0 & 0 \end{pmatrix}^2[p,d]\sum_{\substack{\nu SL \\ \bar{\nu}\bar{S}\bar{L}}} |G^{\nu SL}_{\bar{\nu}\bar{S}\bar{L}}|^2 \times (-1)^L[L]\sum_j (-1)^j[j]\begin{Bmatrix} p & d & j \\ p & k & d \end{Bmatrix}\begin{Bmatrix} \bar{L} & L' & d \\ p & d & L \end{Bmatrix}^2. \tag{23}$$

The expressions above are valid for Sc through Co except Cr and Ni. For Cr, the corresponding expressions are

$$\Delta E_{D,\mathrm{Cr}}(L') = N\sum_k F^k(3p,3d)\begin{pmatrix} p & k & p \\ 0 & 0 & 0 \end{pmatrix}\begin{pmatrix} d & k & d \\ 0 & 0 & 0 \end{pmatrix} \times [p,d]\sum_{\substack{\nu SL \\ \bar{\nu}\bar{S}\bar{L}}} |G^{\nu SL}_{\bar{\nu}\bar{S}\bar{L}}|^2(-1)^{\bar{L}}[L]\begin{Bmatrix} L & L & k \\ d & d & \bar{L} \end{Bmatrix} \times \begin{Bmatrix} L & L & k \\ p & p & L' \end{Bmatrix}, \tag{24}$$

for the direct Coulomb interaction, and

$$\Delta E_{X,\mathrm{Cr}}(L') = N\sum_k G^k(3p,3d)[p,d] \times \begin{pmatrix} p & k & d \\ 0 & 0 & 0 \end{pmatrix}^2\sum_{\substack{\nu SL \\ \bar{\nu}\bar{S}\bar{L}}} |G^{\nu SL}_{\bar{\nu}\bar{S}\bar{L}}|^2[L]\sum_j [j]\begin{Bmatrix} L' & L & j \\ p & d & k \end{Bmatrix} \times \begin{Bmatrix} \bar{L} & L' & j \\ p & d & L \end{Bmatrix}, \tag{25}$$

for the exchange counterpart.

The spin-orbit energy matrices for Sc through Co (excluding Cr) are given by evaluating the matrix

$$\Delta E_{SO}(S'L'J') = N\sum_{\substack{\nu SL \\ \bar{\nu}\bar{S}\bar{L}}} \langle \underline{3p}(\ 3d^{N-1}\bar{\nu}\bar{S}\bar{L}|\}3d^N\nu SL)[S'L'J'] \times |N\varsigma_{3p}\vec{l}\cdot\vec{s}|\underline{3p}(\ 3d^{N-1}\bar{\nu}\bar{S}\bar{L}|\}3d^N\nu SL) \times [S'L'J']\rangle. \tag{26}$$

This evaluates to the expression

$$\Delta E_{SO}(S'L'J') = N[p(p+1)(2p+1)]^{1/2}\varsigma_{3p}[L'] \times \sum_{\substack{\nu SL \\ \bar{\nu}\bar{S}\bar{L}}} |G^{\nu SL}_{\bar{\nu}\bar{S}\bar{L}}|^2[S,L]\begin{Bmatrix} L' & L' & 1 \\ S' & S' & J' \end{Bmatrix} \times \begin{Bmatrix} S' & S' & 1 \\ s_p & s_p & S \end{Bmatrix}\begin{Bmatrix} L & L & 1 \\ p & p & L \end{Bmatrix}, \tag{27}$$

and for Cr, it is

TABLE IV. The FWHM (eV) and maximum strengths (arb. units) for the relative intensity (R), autoionizing intensity (R_A), and the Fano intensity (R_F) using Eqs. (1), (18), and (19), respectively.

	Sc	Ti	V	Cr	Mn	Fe	Co	Ni
R	8.20	8.22	8.69	23.93	10.89	11.18	12.58	13.86
FWHM	2.101	2.101	2.101	2.093	2.101	2.100	2.100	2.099
R_A	8.22	8.23	8.79	23.96	10.90	11.19	12.59	13.87
FWHM	2.084	2.086	2.086	2.082	2.086	2.086	2.086	2.086
R_F	4.60	4.62	4.85	12.87	6.02	6.18	6.92	7.60
FWHM	2.090	2.091	2.093	2.100	2.098	2.099	2.100	2.101

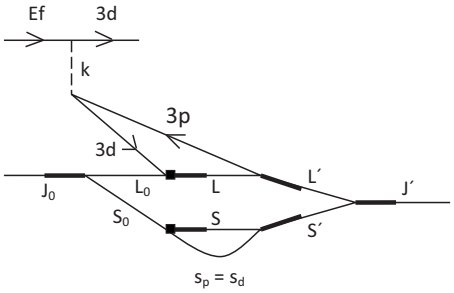

FIG. 5. Amplitude graph for Sc through Ni (excluding Cr).

$$\Delta E_{SO,\mathrm{Cr}}(S'L'J') = N(-1)^{L'-S'+1}[p(p+1)(2p+1)]^{1/2} \times \varsigma_{3p}[S',L']\begin{Bmatrix} J' & L' & S' \\ 1 & S' & L' \end{Bmatrix} \times \sum_{S''}[S'']\begin{Bmatrix} S' & S' & 1 \\ S'' & S'' & s_s \end{Bmatrix} \times \sum_{\nu SL} (-1)^{L+S}|G^{\nu SL}_{\bar{\nu}\bar{S}\bar{L}}|^2 \times \begin{Bmatrix} S'' & S'' & 1 \\ s_p & s_p & S \end{Bmatrix}\begin{Bmatrix} L' & L' & 1 \\ p & p & L \end{Bmatrix}. \quad (28)$$

The direct, exchange, and spin-orbit energy matrices for Ni are obtainable from Eqs. (22), (23), and (27), respectively, by recognizing that $G^{\nu SL}_{\bar{\nu}\bar{S}\bar{L}} \to G^{\nu SL}_{\bar{\nu}\bar{S}\bar{L}}\delta(S,1/2)\delta(L,2)$. If we represent $\Delta E_{ES}(L')$ by the electrostatic energies, and $\Delta E(S'L'J')$ the multiplet energies of the excited configuration states, then

$$\Delta E(S'L'J') = \Delta E_{SO}(S'L'J') - [\Delta E_D(L') - \Delta E_X(L')], \quad (29)$$

where the first minus sign appears because of the $3p$ hole using the inversion rule for shells more than half-filled. Phases involving the p and d electrons in the final expressions for the electrostatic and spin-orbit energy matrices have been extracted.

B. Excitation amplitudes and the electron-energy-loss spectra

Starting with the renormalized diagram of Fig. 1(a), we make the following assignments: $E \to Ef, \varepsilon \to 3d, \varepsilon' \to 3d$, and $i \to 3p$. Then, the $3p3d^{n+1}4s^2$ excited states are coupled to get the final states $S'L'J'$ consistent with the final multiplet states used in the energy diagonalization. Figure 5 shows such coupled states in a graphical representation using the angular momentum graphical techniques of Lindgren and Morrison.[23] An angular momentum line labeled, say, L with a heavy line introduces a factor $[L]^{1/2}$, while a rectangle at the end of such a line introduces the fractional parentage coefficient $G^{\nu SL}_{\bar{\nu}\bar{S}\bar{L}}$. Figure 5 is applicable for the systems Sc through Co (except Cr and Ni). This graph is evaluated using the

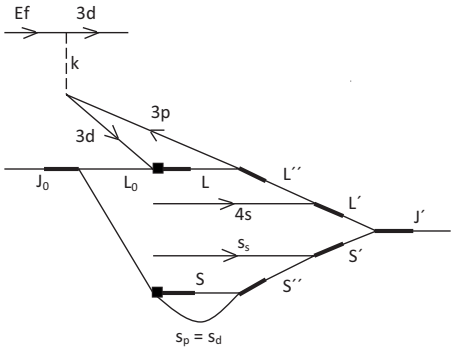

FIG. 6. Amplitude graph for Cr.

theorems of Jucys, Levinson, and Vanagas and the spin offs from the theorems (see, e.g., Sec. 4.1 of Ref. 23). The result is

$$A(S'L'J') = N[d,d,p,f]^{1/2}[J_0,L'/S',J']^{1/2}\delta(S',S_0) \times \sum_k R^k(3d3d,Ef3p)\begin{pmatrix} d & k & f \\ 0 & 0 & 0 \end{pmatrix}\begin{pmatrix} d & k & p \\ 0 & 0 & 0 \end{pmatrix} \times \begin{Bmatrix} J' & k & J_0 \\ L_0 & S' & L' \end{Bmatrix}\sum_{\substack{\nu SL \\ \nu SL}} |G^{\nu SL}_{\bar{\nu}\bar{S}\bar{L}}|[S,L]^{1/2}\begin{Bmatrix} L' & k & L_0 \\ d & L & p \end{Bmatrix}. \quad (30)$$

The expression for Ni is deducible from $A(S'L'J')$ above if $G^{\nu SL}_{\bar{\nu}\bar{S}\bar{L}} \to \delta(L,2)\delta(S,1/2)$ to reduce to

$$A_{\mathrm{Ni}}(S'L'J') = N[d,d,f,p]^{1/2}[J_0,L'/S',J']^{1/2}\delta(L,2)\delta(S,1/2) \times [L,S]^{1/2}\sum_k R^k(3d3d,Ef3p)\begin{pmatrix} d & k & f \\ 0 & 0 & 0 \end{pmatrix} \times \begin{pmatrix} d & k & p \\ 0 & 0 & 0 \end{pmatrix}\begin{Bmatrix} J' & k & J_0 \\ L_0 & S' & L' \end{Bmatrix}\begin{Bmatrix} L' & k & L_0 \\ d & L & p \end{Bmatrix}. \quad (31)$$

In the case of Cr, the graph of the coupled angular momentum states is shown in Fig. 6 and evaluates to the expression

$$A_{\mathrm{Cr}}(S'L'J') = N[d,d,f,p]^{1/2}[J_0/S_0,L',J']^{1/2}\delta(L',L'') \times \sum_k R^k(3d3d,Ef3p)\begin{pmatrix} d & k & f \\ 0 & 0 & 0 \end{pmatrix}\begin{pmatrix} d & k & p \\ 0 & 0 & 0 \end{pmatrix} \times \sum_{\substack{\nu SL \\ \bar{\nu}\bar{S}\bar{L}}} |G^{\nu SL}_{\bar{\nu}\bar{S}\bar{L}}|[S,L]^{1/2}\begin{Bmatrix} L' & k & L_0 \\ d & L & p \end{Bmatrix} \times \sum_j [j]\begin{Bmatrix} J' & k & j \\ L_0 & S' & L' \end{Bmatrix}\begin{Bmatrix} J_0 & s_s & j \\ S' & L_0 & S_0 \end{Bmatrix}. \quad (32)$$

We expect the electron-excited spectra to parallel those of radiative transitions. We therefore impose the following selection rules on the various angular momenta:

$$\Delta S = 0, \quad (33a)$$

TABLE V. The initial and final angular momentum labels for the transitions, as discussed in the text. The Slater integrals $F^2(3p,3d)$, $G^1(3p,3d)$, and $G^3(3p,3d)$, the spin-orbit parameter ς_{3p}, and the total autoionizing and characteristic decay widths Γ are in (eV).

	S_0	L_0	J_0	S'	L'	J'	F^2	G^1	G^3	ς_{3p}	Γ
					1	1/2, 3/2					
Sc	1/2	2	3/2	1/2	2	3/2, 5/2	8.06	10.05	5.99	0.29	6.80
					3	5/2					
					2	1, 2, 3					
Ti	1/2	2	3/2	1/2	3	2, 3	9.12	11.41	6.83	0.83	8.02
					4	3					
					2	1/2, 3/2					
V	3/2	3	3/2	3/2	3	5/2	9.97	12.47	7.49	0.48	8.84
					4	3/2, 5/2					
Cr	3	0	3	3	1	2, 3, 4	9.85	12.29	7.33	0.59	8.43
Mn	5/2	0	5/2	5/2	1	3/2, 5/2, 7/2	11.51	14.36	8.66	0.74	9.79
					1	3					
Fe	2	2	4	2	2	3, 4	12.12	15.08	9.10	0.90	9.52
					3	3, 4, 5					
Co	1	3	9/2	1	3	7/2	12.76	15.85	9.57	0.90	9.52
					4	7/2, 9/2					
Ni	1	3	4	1	2	3	12.76	15.85	9.57	0.90	9.46
					3	3, 4	13.41	16.62	10.05	1.31	

$$\Delta L = 0, \pm 1, \quad L_0 + L' \geqslant 1, \tag{33b}$$

$$\Delta J = 0, \pm 1, \quad J_0 + J' \geqslant 1. \tag{33c}$$

With the above conditions, the accessible final states used in the calculation of the energy matrices are displayed in Table V. Also shown in Table V are the Slater integrals and the $3p$ spin-orbit interaction parameters used in the multiplet energy calculations.

We extend the analysis of the inelastic electron scattering on atoms in the Bethe–Born approximation for $4d \rightarrow 4f$ transitions in La^{3+} and Ce^{3+} to the $3p \rightarrow 3d$ transitions in the present case.[17] Equation (2.24) in that work indicates that the correlation part of the atomic form factor can be written as

$$F_{Born}^{corr}(q,\varepsilon) = 1 - W(q,\varepsilon) \sum_{S'L'J'} \sum_{k} \frac{g_k(S'L'J')R^k(3d3d,\varepsilon f3p)}{E(S'L'J') - \varepsilon - i\delta}, \tag{34}$$

where $g_k(S'L'J')$ is the coupling angular factor with

$$W(q,\varepsilon) = \sum_{\nu} \int dr P_{3d}(r) j_\nu(qr) \times P_{3p}(r) \Big/ \sum_{\nu} \int dr P_{\varepsilon d}(r) j_\nu(qr) P_{3p}(r), \tag{35}$$

and $j_\nu(qr)$ is a spherical Bessel function of integral order ν. In the present application, we have taken $P_{\varepsilon d} = P_{3d}$ making $W(q,\varepsilon) = 1$. This removes the q dependence of (where q here refers to the momentum transfer of the impinging electron to the atom) the Born correlation form factor and

$$F_{Born}^{corr}(q,\varepsilon) \rightarrow F_{Born}^{corr}(\eta) = 1 + \sum_j \frac{a_j}{\eta - E_j + i\Gamma/2}. \tag{36}$$

In the above, we have made the assignments $j \rightarrow S'L'J'$, $a_j \rightarrow A(S'L'J') = \Sigma_k g_k(S'L'J')R^k(3d3d,\varepsilon f3p)$, and $E_j \rightarrow \Delta E(S'L'J')$. Thus, the relative electron-energy-loss intensity $I(\eta)$ for the excitation is given by the dimensionless expression

$$I(\eta) = |F_{Born}^{corr}(\eta)|^2, \tag{37}$$

where the energy loss parameter η is defined as

$$\eta = E - E_{3d} - E_{3d} + E_{3p} - \mathrm{Re}[S_d(E)], \tag{38}$$

and the FWHM parameter Γ is determined from the autoionizing and characteristic decay widths Γ_a and Γ_c, respectively, and given by

$$\Gamma = \Gamma_a + \Gamma_c = 2\pi[(v_{DE})^2 + (v_E'')^2]. \tag{39}$$

The electron-energy-loss spectra reported in Fig. 7 are calculated using $I(\eta)$ above, and Γ was evaluated at the $3p \rightarrow 3d$ excitation edge. These values are also reported in Table V. The coefficients of fractional parentage $G_{\bar{\nu}\bar{S}\bar{L}}^{\nu SL}$ used in the numerical computations were taken from Ref. 24 for Sc

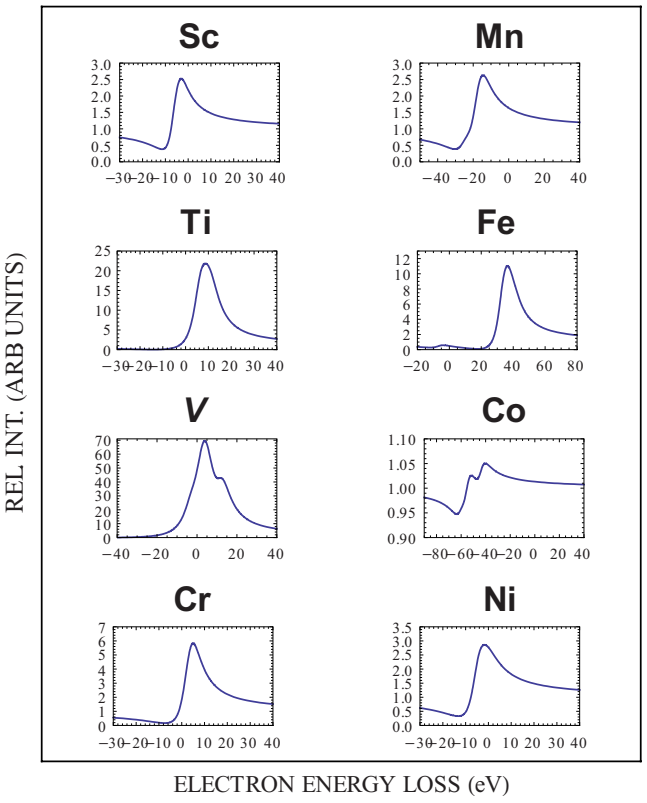

FIG. 7. (Color online) The relative intensities (arb. units) for the TMs using $I(\eta)$ from Eq. (37).

through Co, and those for Ni from Ref. 25. We report in Table VI the extracted FWHM of the spectra in Fig. 7 by fitting to a Lorentzian or Gaussian distribution along with the maximum heights. Also reported are the multiplet widths Δ, the difference between the highest and lowest multiplet energies.

V. DISCUSSION

In the application of the theoretical formalism to the lanthanides La and Ce,[16] contributions from the ladder diagrams to the scattering amplitude outweighed those from the ring diagrams. In the present application to the TMs, they are the ring diagrams that rather dominate the contributions. This interchange of roles is rooted in the coupling of the angular momenta in the integration or summation over the magnetic angular (m_l) and the magnetic spin (m_s) quantum numbers to obtain the Slater integrals $R^{1,3,5}(4f4f,4dkg)$ for La and Ce and $R^{1,3}(3d3d,3pkf)$ for the TMs. Obviously, the TMs with the smaller set of $|m_l|$ values provide larger angular coefficients than the lanthanides with larger set of $|m_l|$ values.

Two experimental groups have made electron-energy-loss measurements near the $3p$ excitation threshold of the TMs using the same type of equipment, and under nearly identical conditions as possible. The early group, Robins and Swan,[15] recorded their measurements for V through Cu, while the second group, Zajac *et al.*,[3] made their measurements for Sc through Cu. The former group has had their data readjusted to have the highest peak in each spectrum to have the same intensity value of eight units. Intensitywise, the data would be unsuitable for comparison with the present calculations that emphasize on the variation of the highest intensity peak across the TMs. This leaves the latter group's measurements to compare with the theoretical calculations. A major characteristic trend that they reported was that their measurements portrayed emission intensity structures that decreased with increasing Z, for the low Z-end group members (Sc to Cr) and for the high Z-end members (Mn to Cu). These observations are clearly seen in Fig. 4 of their work.

Now, we turn to the theoretical results. We find that the energy-loss spectra in Fig. 4 with only electrostatic interactions are completely different from the spectra in Fig. 7 with electrostatic and magnetic effects, both in intensity and spectral widths. Table IV shows that the spectral widths are basically the same across the TM series with a value of about 2.1 eV with varying intensities that are about the same for Sc, Ti, and V (albeit increasing), and increasing gradually for Mn through Ni. Cr sets a demarcation between these two groupings and is about thrice as intense as the low Z-end group members (Sc-V) and about twice as intense as the high Z-end group members (Mn-Ni). Table VI, on the other hand, shows spectral widths spanning about 6–17 eV across the TM series when magnetic effects are incorporated. It should be pointed out that no scaling was implemented to the Slater integrals, spin-orbit parameters, and the continuum Slater integrals used in the calculation of the multiplets and the excitation amplitudes. We note in passing that while the multiplet splitting Δ varies from several electron volts to the maximum realized in Fe of about 47 eV, the interference between the different multiplet channels in taking the absolute value of the excitation amplitude brings the FWHM to within the measured values. It is also worth mentioning that if all the TMs were prepared under the same conditions, the present theory predicts that the structure for Co would have the smallest intensity and the broadest width in comparison with the rest of the others in the TM series. Also, apart from the unusually large intensity exhibited by Fe in comparison with the rest of the TMs, one of its multiplets is pushed far to the low energy end of the loss spectrum emerging as a speck. We

TABLE VI. The multiplet spread, Δ, the full width at half maximum (FWHM), and the maximum height extracted from the energy loss spectra in Fig. 7 using a Lorentzian or a Gaussian fit.

	Sc	Ti	V	Cr	Mn	Fe	Co	Ni
Δ (eV)	2.30	5.60	14.34	1.69	9.06	46.78	16.73	3.99
FWHM (eV)	6.36	8.26	13.81	7.44	9.15	12.09	17.31	8.37
Height (arb. units)	2.50	21.18	67.07	5.82	2.62	10.80	1.05	2.83

find from Table VI that there is no inherent trend in the variation of the intensity structures across the TM series, as reported in Ref. 3. On the other hand, Ref. 15 had reported energy-loss spectra of varying intensities, spectral widths, and structures akin to the observations of Ref. 3. It is rather unfortunate that the data of Ref. 15 had been normalized to have the same peak values, thereby making it unsuitable to compare with the peak variations in the present calculations. Nevertheless, a cursory look at the spectral widths of the experimental data of both Refs. 15 and 3 seem to reflect the numbers that theory provides. More importantly, to obtain spectral widths that approach the measured values, it is apparent that magnetic effects are indispensable. This does not mean that the theoretical description in Sec. II and the associated results are redundant. Moreover, while the FWHM experimental values can be gauged to be far larger than the uniform value of about 2.1 eV predicted for Sc through Ni in Table IV, this theoretical value is in conformity with 2.0 ± 0.2 eV that was used as a fit to the experimental line shape using a Fano-type formula by Dietz *et al.*[1] Finally, we see from Table IV that for the TMs, the contributions from the ladder diagrams to the autoionizing amplitude could be neglected with little effect to the intensity. The application of the theoretical formulations to the $3d$ excitation edge of the lanthanides and the $2p$ excitation edge of the TMs is in progress.

ACKNOWLEDGMENT

Partial support from Kent State University's Research Council is gratefully acknowledged.

*knuroh@kent.edu

[1] R. E. Dietz, E. G. McRae, Y. Yafet, and C. W. Caldwell, Phys. Rev. Lett. **33**, 1372 (1974).
[2] S. D. Bader, G. Zajac, and J. Zak, Phys. Rev. Lett. **50**, 1211 (1983).
[3] G. Zajac, S. D. Bader, A. J. Arko, and J. Zak, Phys. Rev. B **29**, 5491 (1984).
[4] D. H. Pearson, B. Fultz, and C. C. Ahn, Appl. Phys. Lett. **53**, 1405 (1988).
[5] R. D. Leapman and L. A. Grunes, Phys. Rev. Lett. **45**, 397 (1980).
[6] R. E. Dietz, E. G. McRae, and J. H. Weaver, Phys. Rev. B **21**, 2229 (1980).
[7] T. Jach and C. J. Powell, Solid State Commun. **40**, 967 (1981).
[8] A. P. Hitchcock and C. H. Teng, Surf. Sci. **149**, 558 (1984).
[9] M. Kurahashi, M. Yamanoto, and S. Naito, J. Phys.: Condens. Matter **7**, L463 (1995).
[10] K. Berndt, C. Wenzel, T. Dörre, T. Herzel, and A. Neumann, Phys. Status Solidi B **104**, K49 (1981).
[11] L. Lozzi, M. Passacantando, P. Picozzi, S. Santucci, M. Diociaiuti, and M. de Crescenzi, Solid State Commun. **83**, 921 (1992).
[12] L. C. Davis and L. A. Feldkamp, Phys. Rev. A **17**, 2012 (1978).
[13] L. C. Davis and L. A. Feldkamp, Phys. Rev. B **23**, 6239 (1981).
[14] R. D. Leapman, L. A. Grunes, and P. L. Fejes, Phys. Rev. B **26**, 614 (1982).
[15] J. L. Robins and J. B. Swan, Proc. Phys. Soc. London **76**, 857 (1960).
[16] K. Nuroh, Phys. Rev. B **70**, 205115 (2004).
[17] K. Nuroh, J. Phys. C **20**, 5305 (1987).
[18] C. Froese Fischer, T. Brage, and P. Jönsson, *Computational Atomic Structure: An MCHF Approach* (Institute of Physics, Bristol, 1997).
[19] N. Vaeck, M. Godefroid, and J. E. Hansen, J. Phys. B **24**, 361 (1991).
[20] T. Brage, C. Froese Fischer, and N. Vaeck, J. Phys. B **26**, 621 (1993).
[21] G. Miecznik, T. Brage, and C. Froese Fischer, Phys. Rev. A **47**, 3718 (1993).
[22] M. Galassi, J. Davies, J. Theiler, B. Gough, G. Jungman, M. Booth, and F. Rossi, *GNU Scientific Library Reference Manual*, 2nd ed. (Network Theory Group, Bristol, 2005).
[23] I. Lindgren and J. Morrison, *Atomic Many-Body Theory* (Springer-Verlag, Berlin, 1986).
[24] C. W. Nielson and G. F. Koster, *Spectroscopic Coefficients for p^n, d^n, and f^n, Configurations* (M.I.T. Press, Cambridge, 1963).
[25] R. D. Cowan, *The Theory of Atomic Structure and Spectra* (University of California Press, Berkeley, 1981).